

Interaction between thermal convection and mean flow in a rotating system with a tilted axis

Naoaki Saito¹‡ and Keiichi Ishioka¹

¹Graduate School of Science, Kyoto University, Kitashirakawa Oiwake-cho, Sakyo-ku, Kyoto 606-8502, JAPAN

E-mail: naoaki@kugi.kyoto-u.ac.jp

Abstract. Thermal convection in a sine-type horizontal shear flow in a rotating system with a rotation axis tilted from the vertical direction is investigated, sweeping three parameters: the Taylor number, the tilt angle of the rotation axis (i.e., latitude), and the Rayleigh number. Nonlinear time evolutions show that there is not only a regime in which roll convections of a herringbone pattern accelerate a mean flow but that there is also a regime in which a large-scale east–west roll convection accelerates the mean flow strongly. The parameter region in which this type of stable steady two-dimensional roll solution exists is determined by linear stability analyses. Even when the two-dimensional steady solution is not linearly stable, unsteady quasi-periodic solutions oscillating around the steady solution can be found in the nonlinear time evolutions. Finally, a simple mechanism for the acceleration of the mean flow by the large-scale east–west roll convection is described in detail, in which both the tilt of the rotation axis and the sine-type horizontal shear of the flow are important.

Keywords: Thermal Convection, Horizontal Shear Flow, Rotating System, Tilted Axis

‡ Corresponding author: naoaki@kugi.kyoto-u.ac.jp

1. Introduction

Thermal convection is an important type of motion in geophysical fluids. Spatial variation of the background flow field plays an important role in determining the pattern of thermal convection in the atmosphere, which is not the case in laboratory experiments. Several studies have examined thermal convection in vertical shear flows with the intention of applying the obtained results to the real atmosphere. For example, Asai (1970) studied thermal convection in a plane Couette flow numerically. However, there have been few studies on thermal convection in horizontal shear flows. Davies-Jones (1971) is one of the early studies of this sort. He performed linear stability analysis to show that roll convection with the axis parallel to the basic flow is preferred in a horizontal plane Couette flow. While the preceding paper excluded system rotation, Yoshikawa and Akitomo (2003) treated thermal convection in a horizontal plane Couette flow in a rotating system and demonstrated through computing nonlinear time evolutions that roll convection with the axis tilted from the direction of the basic flow is formed during the transition from cellular convection to roll convection parallel to the basic flow. Thermal convections in sine-type horizontal shear flow in a rotating system were investigated by Furukawa and Niino (2006), who demonstrated that a barotropic eddy of wavenumber 1 is formed in the late stage of nonlinear time evolutions. Their energy analysis revealed that the barotropic eddy is generated by the kinetic energy conversion from baroclinic components to the barotropic eddy. However, the generation mechanism of the eddy was not explained, nor did the energy conversion from the mean flow to the barotropic eddy appear to be negligible. Therefore, Saito and Ishioka (2008) performed not only nonlinear time evolutions but also a linear stability analysis to examine the formation process of the barotropic eddy of wavenumber 1 in detail. They demonstrated that barotropic instability plays the most important role in the generation of the barotropic eddy.

When thermal convections in planetary atmospheres are treated, effects caused by the condition whereby the vertical direction is not parallel to the planetary rotation axis, except at the poles, must be considered. Momentum transport by thermal convections in a system with a tilted rotation axis (we hereinafter refer to such a system as a tilted f -plane) has been attracting attention because this type of transport may account for the zonal flow profile of the Sun obtained by the recent helioseismology (see Miesch (2000) for a detailed review). Studies of thermal convection on a tilted f -plane date back to the linear stability analyses conducted by Chandrasekhar (1961). Nonlinear time evolution of convections on a tilted f -plane was performed by Hathaway and Somerville (1983), who demonstrated that the horizontal component of the rotation vector elongates the convection cells in a north–south direction and tends to turn upward motions to the west and downward motions to the east in a manner that produces a large-scale circulation. Julien and Knobloch (1998) examined the linear stability problem as well as the strongly nonlinear problem for convections on a tilted f -plane in detail. They evaluated the second-order acceleration by the linearly unstable mode, which yields good agreement

with the results reported by Hathaway and Somerville (1983).

Considering the giant planets, such as Jupiter, the effects of both the horizontal shear of the mean flow and the tilt of the rotation axis should be taken into account. However, there are remarkably few studies that deal with both of these effects. Hathaway and Somerville (1987) treated thermal convection in an eastward sine-type horizontal shear flow on a tilted f -plane, with low latitudes of a rotating planet in mind. They showed that the roll convections of a herringbone pattern accelerate the mean flow by computing nonlinear time evolutions. However, they reached their conclusions based on a simple energy analysis of the final state of the evolution. Therefore, Saito and Ishioka (2009) performed both nonlinear time evolution and a linear stability analysis with a setting similar to that of Hathaway and Somerville (1987). They examined the acceleration mechanism of the mean flow in detail to show that the Coriolis force on the second-order vertical flow associated with the linearly unstable mode has the most important effect on the acceleration. However, the parameter space they explored was not so wide.

In the present paper, nonlinear time evolutions of thermal convection in a sine-type horizontal shear flow on a tilted f -plane are conducted, sweeping widely the following three parameters: the Taylor number, the tilt angle of the rotation axis (i.e., the latitude), and the Rayleigh number. The remainder of the present paper is organized as follows. The numerical model is described in detail in section 2. The results of nonlinear time evolutions are shown in section 3. The analysis of the acceleration mechanism of the mean flow is presented in section 4. Finally, the summary and discussion are presented in section 5.

2. Model equations and computing configurations

2.1. Basic equations

We assume a Boussinesq fluid in a system rotating around a rotation axis with an angular velocity of $f/2$. The basic equations are nondimensionalized using the following dimensional variables: depth in the vertical direction, kinematic viscosity, and the difference in buoyancy between the top and bottom boundaries. The equation of motion, the thermal equation, and the continuity equation are as follows:

$$\frac{\partial \mathbf{u}}{\partial t} + (\mathbf{u} \cdot \nabla) \mathbf{u} = -\nabla p - \mathbf{f} \times (\mathbf{u} - \mathbf{u}_B) + Ra \mathbf{b} + \nabla^2 (\mathbf{u} - \mathbf{u}_B), \quad (2.1)$$

$$\frac{\partial b}{\partial t} + (\mathbf{u} \cdot \nabla) b = w + \nabla^2 b, \quad (2.2)$$

$$\frac{\partial u}{\partial x} + \frac{\partial v}{\partial y} + \frac{\partial w}{\partial z} = 0, \quad (2.3)$$

where

$$\mathbf{u} = \begin{pmatrix} u \\ v \\ w \end{pmatrix}, \quad \mathbf{f} = \begin{pmatrix} f \cos \theta \\ 0 \\ f \sin \theta \end{pmatrix}, \quad \mathbf{b} = \begin{pmatrix} 0 \\ 0 \\ b \end{pmatrix},$$

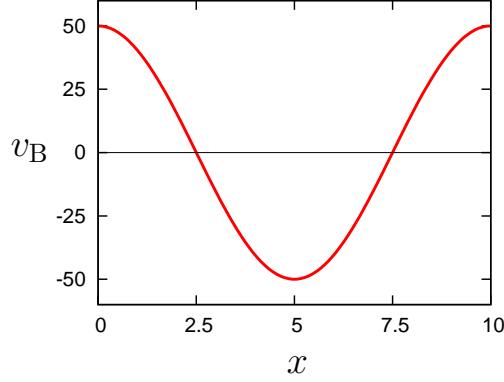


Figure 1. Basic flow profile. The horizontal axis is x , and the vertical axis is the fluid velocity in the y direction, $v_B(x)$.

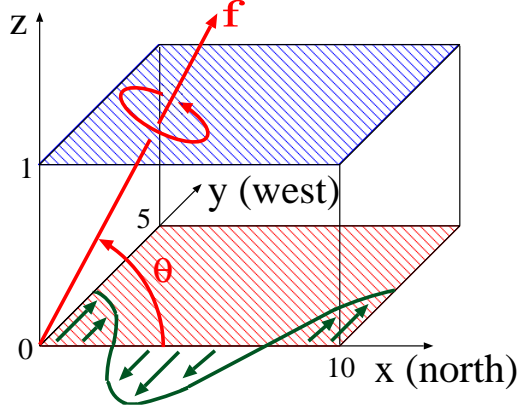


Figure 2. Schematic diagram of the model configuration.

$$\mathbf{u}_B = \begin{pmatrix} 0 \\ v_B \\ 0 \end{pmatrix}, \quad v_B = V_0 \cos\left(\frac{2\pi}{L_x}x\right), \quad (2.4)$$

where t is time, (x, y, z) are the Cartesian coordinate directions (z is the vertical direction), \mathbf{u} is the velocity vector, p is the pressure function, \mathbf{f} is the rotation vector, Ra is the Rayleigh number, b is the buoyancy, ∇^2 is the Laplacian, θ is the tilt angle of the rotation axis, i.e., latitude ($0 \leq \theta \leq \pi/2$), \mathbf{u}_B is the basic flow (a horizontal shear flow), V_0 is the maximum speed of the basic flow, and L_x is the nondimensionalized length of the domain in the x direction. The basic flow profile is shown in figure 1. The terms \mathbf{u}_B in the right-hand side of (2.1) are included in order to make the basic flow a steady solution. The Prandtl number is set to 1, following Hathaway and Somerville (1987) and Furukawa and Niino (2006). A schematic diagram of the model is shown in figure 2.

Here, we describe the relationship between the nondimensional and dimensional

parameters. The Rayleigh number and the Taylor number are given as follows:

$$Ra = \frac{\alpha g \Gamma d^4}{\kappa \nu}, \quad Ta = \frac{f^2 d^4}{\nu^2}, \quad (2.5)$$

where α is the coefficient of thermal expansion, g is the gravitational acceleration, $\Gamma = (T_1 - T_2)/d$ is the temperature lapse rate, T_1 and T_2 are the temperatures of the bottom and top boundaries ($T_1 > T_2$), respectively, d is the depth in the vertical direction, κ is the coefficient of thermal diffusivity, and ν is the kinematic viscosity. The relationship between temperature $T(x, y, z, t)$ and nondimensional buoyancy $b(x, y, z, t)$ is

$$T(x, y, z, t) = T_1 + \Gamma [b(x, y, z, t) d - z]. \quad (2.6)$$

Note that in the following sections $T(x, y, z, t)$ fields are shown instead of $b(x, y, z, t)$ fields in figures, where we set $\alpha = g = d = \kappa = \nu = 1$, $T_1 = Ra$, and $T_2 = 0$ for convenience. In this setting, the Taylor number is simplified as $Ta = f^2$.

2.2. Vorticity equation

The vorticity equation is derived from (2.1) and (2.3):

$$\frac{\partial \boldsymbol{\omega}}{\partial t} = \nabla \times [\mathbf{u} \times (\boldsymbol{\omega} + \mathbf{f})] + \nabla \times (\mathbf{f} \times \mathbf{u}_B) + Ra (\nabla \times \mathbf{b}) + \nabla^2 (\boldsymbol{\omega} - \boldsymbol{\omega}_B), \quad (2.7)$$

where

$$\boldsymbol{\omega} = \begin{pmatrix} \omega_1 \\ \omega_2 \\ \omega_3 \end{pmatrix} = \nabla \times \mathbf{u}, \quad \nabla \times (\mathbf{f} \times \mathbf{u}_B) = \begin{pmatrix} 0 \\ -f \cos \theta \frac{\partial v_B}{\partial x} \\ 0 \end{pmatrix},$$

$$\boldsymbol{\omega}_B = \begin{pmatrix} 0 \\ 0 \\ \omega_{3B} \end{pmatrix}, \quad \omega_{3B} = \frac{\partial v_B}{\partial x} = -\frac{2\pi V_0}{L_x} \sin\left(\frac{2\pi}{L_x} x\right), \quad (2.8)$$

where $\boldsymbol{\omega}$ is the vorticity vector, and $\boldsymbol{\omega}_B$ is the vorticity vector corresponding to the basic flow. Since $\nabla \cdot \boldsymbol{\omega} = 0$, only two of the three vorticity components are independent. We can calculate the nonlinear time evolution of two independent components of the vorticity and buoyancy based on (2.7) and (2.2).

2.3. Boundary conditions

We assume periodic boundary conditions in both the x and y directions. The periods are L_x and L_y for the x and y directions, respectively. The boundary condition at $z = 0, 1$ is free-slip and fixed temperature. In other words,

$$\frac{\partial u}{\partial z} = \frac{\partial v}{\partial z} = w = b = \omega_1 = \omega_2 = \frac{\partial \omega_3}{\partial z} = 0 \quad \text{at } z = 0, 1. \quad (2.9)$$

2.4. Computational methods

The Fourier–Legendre spectral method is used for the space discretization of the dependent variables. We use the Fourier expansion in the x and y directions and the Legendre polynomial expansion in the z direction. The details of the expansion are shown in Appendix A. The truncation wavenumbers in the x , y , and z directions are 21, 21, and 20, respectively. The number of grids for the spectral transform method is $64 \times 64 \times 32$. The classical fourth-order Runge–Kutta scheme is used for the time integration.

2.5. Parameter settings

We set the parameter values following Hathaway and Somerville (1987). The maximum speed of the basic flow is set as $V_0 = 50$. The size of the computational domain is set as $L_x = 10$, $L_y = 5$. Here, we set $L_y = 5$ in order to suppress the barotropic instability of the basic flow. If we set $L_y = 10$ according to Hathaway and Somerville (1987), the barotropic instability of the basic flow obscures the details of the interaction between convection and the mean flow (Saito and Ishioka (2008)). The Taylor number, $Ta = f^2$, is swept in the range of 10^4 , 3×10^4 , and 10^5 . The tilt angle of the rotation axis, θ , is swept in the range of 15° , 30° , 45° , 60° , and 75° . In Appendix B, we discuss the relevance of the values of V_0 and Ta chosen in this manuscript compared with the Jupiter atmosphere. We conduct 51 numerical experiments, changing Ra for each pair of Ta and θ , which means that the total number of numerical experiments is $3 \times 5 \times 51 = 765$. We choose the parameter sweep range of Ra depending on the values of Ta and θ in order to distinguish the flow regimes of the end states of the time evolutions. Please refer to figures 11, 14, and 15 to see the swept range of the value of Ra .

2.6. Calculations of the critical Rayleigh number

Before conducting the numerical experiments, we perform linear stability analyses repeatedly with the various Ra to search for the critical Rayleigh number, Ra_c , at which the growth rate is $\sigma = 0$. For reference, we also calculate the case of $\theta = 0^\circ$ and 90° as well as the case of $Ta = 0$. Table 1 shows Ra_c and the critical wavenumber m_c with respect to the disturbance of $m \neq 0$, i.e., the roll convections of a herringbone pattern, and table 2 shows Ra_c with respect to the disturbance of $m = 0$, i.e., roll convections parallel to the y axis. Here, m is the wavenumber in the y direction. Note that Ra_c is independent of θ when $Ta = 0$ and the value of Ra_c for $Ta = 0$ is listed only for $\theta = 0^\circ$ in tables 1 and 2.

In the cases of $\theta = 75^\circ$ and 90° , $Ra_c(m = 0)$ is slightly smaller than $Ra_c(m \neq 0)$, which means that roll convections parallel to the y axis appear first. This is because the roll convections parallel to the mean flow are preferred in the horizontal shear flow. On the other hand, in the cases of $\theta = 0^\circ$, 15° , 30° , 45° , and 60° , $Ra_c(m \neq 0)$ is smaller than $Ra_c(m = 0)$, which means that roll convections of a herringbone pattern appear first

Table 1. Critical Rayleigh number and critical wavenumber with respect to the disturbance of $m \neq 0$ for seven values of θ and four values of Ta .

| $Ta \backslash \theta$ | 0° | 15° | 30° | 45° | 60° | 75° | 90° |
|------------------------|---------------|---------------|----------------|----------------|----------------|----------------|----------------|
| 0 | 876.1 (1) | – – | – – | – – | – – | – – | – – |
| 10^4 | 1955.3 (2) | 2421.9 (3) | 3338.5 (3) | 4244.1 (4) | 4944.4 (4) | 5441.7 (4) | 5620.6 (4) |
| 3×10^4 | 2781.6 (3) | 3732.8 (3) | 5614.2 (4) | 7671.4 (5) | 9120.0 (5) | 10150.4 (5) | 10516.0 (5) |
| 10^5 | 4156.3 (3) | 6404.6 (4) | 10618.5 (5) | 15079.3 (6) | 18683.5 (6) | 21224.9 (6) | 21959.3 (7) |

Table 2. Critical Rayleigh number and critical wavenumber with respect to the disturbance of $m = 0$ for seven values of θ and four values of Ta .

| $Ta \backslash \theta$ | 0° | 15° | 30° | 45° | 60° | 75° | 90° |
|------------------------|-----------|------------|------------|------------|------------|------------|------------|
| 0 | 671.4 | – | – | – | – | – | – |
| 10^4 | 7055.5 | 8328.5 | 7980.4 | 7564.1 | 5858.2 | 4943.7 | 4659.2 |
| 3×10^4 | 18691.6 | 22035.3 | 18986.6 | 15328.9 | 11753.0 | 9972.4 | 9433.6 |
| 10^5 | 63890.7 | 58812.0 | 45038.1 | 32234.4 | 24998.8 | 21502.6 | 20455.4 |

as Ra increases. Mechanism of emergence of roll convections of a herringbone pattern can be explained as follows. Without a basic flow, roll convections the axis of which is parallel to the x axis are preferred due to the Taylor-Proudman effect. The existence of the upper and the lower boundaries prevents the roll axis from being parallel to the rotation axis. With a basic flow, the roll convections are localized in the weak shear regions and distorted by the horizontal advection, which leads to a herringbone pattern. When the rotation axis tilts sufficiently and the Taylor-Proudman effect exceeds the shear effect that prefers roll convections parallel to the y axis, a herringbone pattern emerges. The smaller Ra_c of the two tables is hereinafter referred to as the critical Rayleigh number.

Figure 3 shows the dependence of Ra_c on $f \sin \theta$, which is the vertical component of the rotation vector. Here, $f = \sqrt{Ta}$. Most all the plots in figure 3 reside approximately on a curve. This is because, if there were no basic flow, the critical Rayleigh number should be determined by the vertical component of the rotation vector, as pointed out by Chandrasekhar (1961).

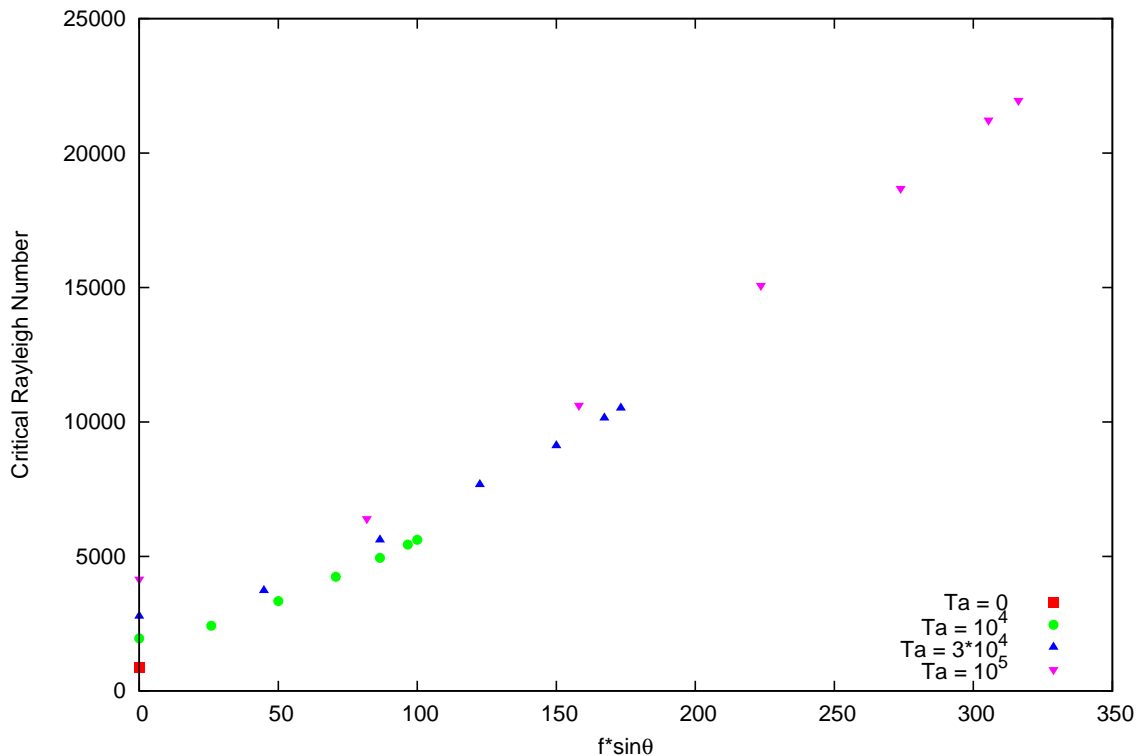


Figure 3. The dependence of the critical Rayleigh number (vertical axis) on $f \sin \theta$ (horizontal axis). The red square, green circles, blue triangles, and purple upside-down triangles indicates the data for $Ta = 0$, $Ta = 10^4$, $Ta = 3 \times 10^4$, and $Ta = 10^5$, respectively.

2.7. Adequacy of the numerical solutions

We examine the adequacy of the numerical solutions by changing the spacial resolutions of the numerical model (doubling the resolutions in x , y , and z directions). It is found that the numerical solutions obtained with the original resolutions do not differ those with higher resolutions qualitatively even when Ra is the largest in the range we sweep.

3. Nonlinear time evolution—parameter-sweep experiment

We compute nonlinear time evolutions from an initial state, $\mathbf{u} = \mathbf{u}_B$ and $b = b_{\text{perturb}}$, sweeping Ta , θ , and Ra , in the manner described in section 2.5. Here, b_{perturb} is the initial perturbation on the buoyancy field that is set as follows:

$$b_{\text{perturb}}(x_i, y_j, z_k) = \begin{cases} 10^{-10} & (x_i = 0, y_j = 2.5, z_k = 0.5), \\ 0 & (\text{else}), \end{cases} \quad (3.1)$$

where (x_i, y_j, z_k) is the coordinate value of each grid. An example of the time evolution is given in figure 4, which shows x - y sectional views of the temperature fields for $Ta = 10^4$, $\theta = 45^\circ$, and $Ra = 7,000$ at $t = 0.0, 1.5, 2.0, 4.0, 6.0,$ and 10.0 . Since the initial perturbation is imposed at $x = 0$ (figure 4(a)), the linear eigenmode of a

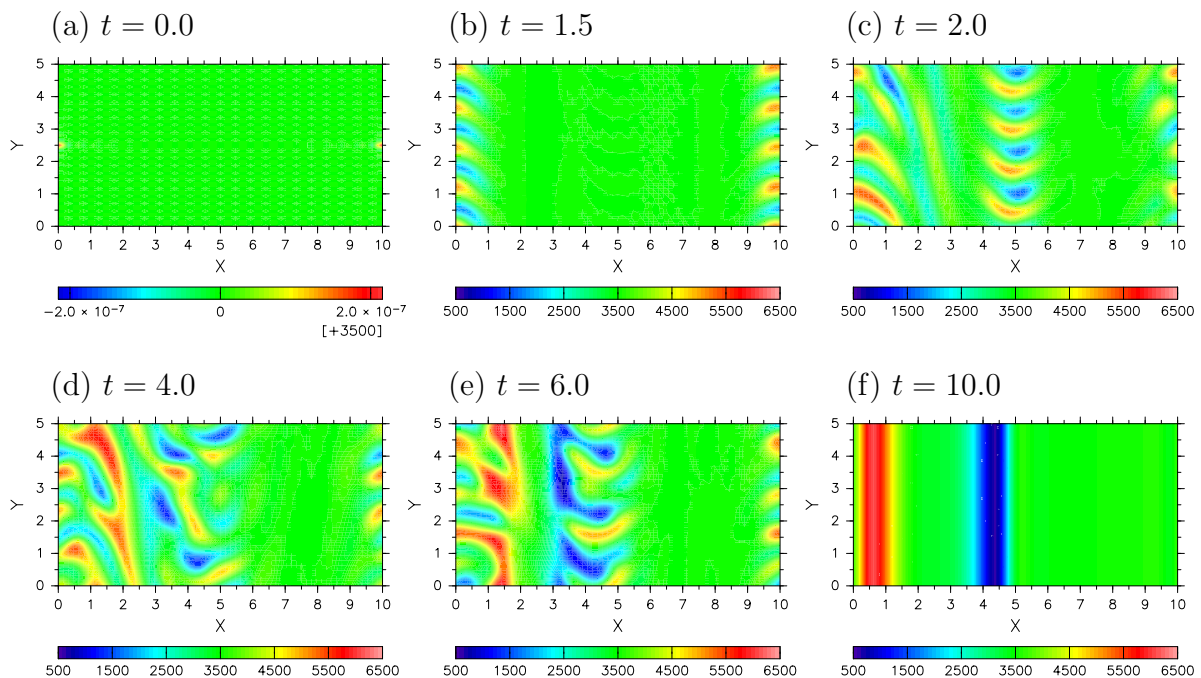


Figure 4. Snapshots of the nonlinear time evolution for the case in which $Ta = 10^4$, $\theta = 45^\circ$, and $Ra = 7,000$. x - y sectional views of the temperature fields at $z = 0.5$ are given. (a) $t = 0.0$, (b) $t = 1.5$, (c) $t = 2.0$, (d) $t = 4.0$, (e) $t = 6.0$, and (f) $t = 10.0$.

herringbone pattern with a peak at $x = 0$ grows first (figure 4(b)). Then, the other eigenmode with a peak at $x = 5$, which has the same growth rate as the preceding eigenmode, also grows to have a finite amplitude (figure 4(c)). After the interaction between the two eigenmodes makes the flow turbulent (figure 4(d)), the temperature field changes considerably to eventually yield a 2D (i.e., y -independent) pattern (figures 4(e) and 4(f)). Figure 5 shows an x - z sectional view of the temperature field and the profile of zonally and vertically averaged zonal velocity $\langle \bar{v} \rangle(x)$, as well as an x - y sectional view of the temperature field for the final state shown in figure 4(f) ($t = 10.0$). As shown in figure 5(b), the 2D pattern of the x - y sectional view of the temperature field is the manifestation of a large-scale convective roll rising near $x = 0.5$ and descending near $x = 4.5$. Corresponding to the appearance of the large-scale convective roll, strong acceleration is observed in the $\langle \bar{v} \rangle(x)$ profile (figure 5(c)).

The final states differ depending on the sweeping parameters. Figure 6 shows the final state for $Ta = 10^4$, $\theta = 45^\circ$, and $Ra = 9,300$. In this case, the temperature field has wavenumber components of 2 and 3 (figure 6(a)). However, as shown in the x - z sectional view (figure 6(b)), a large-scale roll convection is dominant, and strong acceleration is observed in the $\langle \bar{v} \rangle(x)$ profile (figure 6(c)), which is similar to the case of figure 5.

Large-scale roll convection is not always observed for all of the parameter ranges. When Ra is small, remnants of linear eigenmodes can be observed even in the final states. Figure 7 shows the final state for $Ta = 10^4$, $\theta = 30^\circ$, and $Ra = 5,000$, in

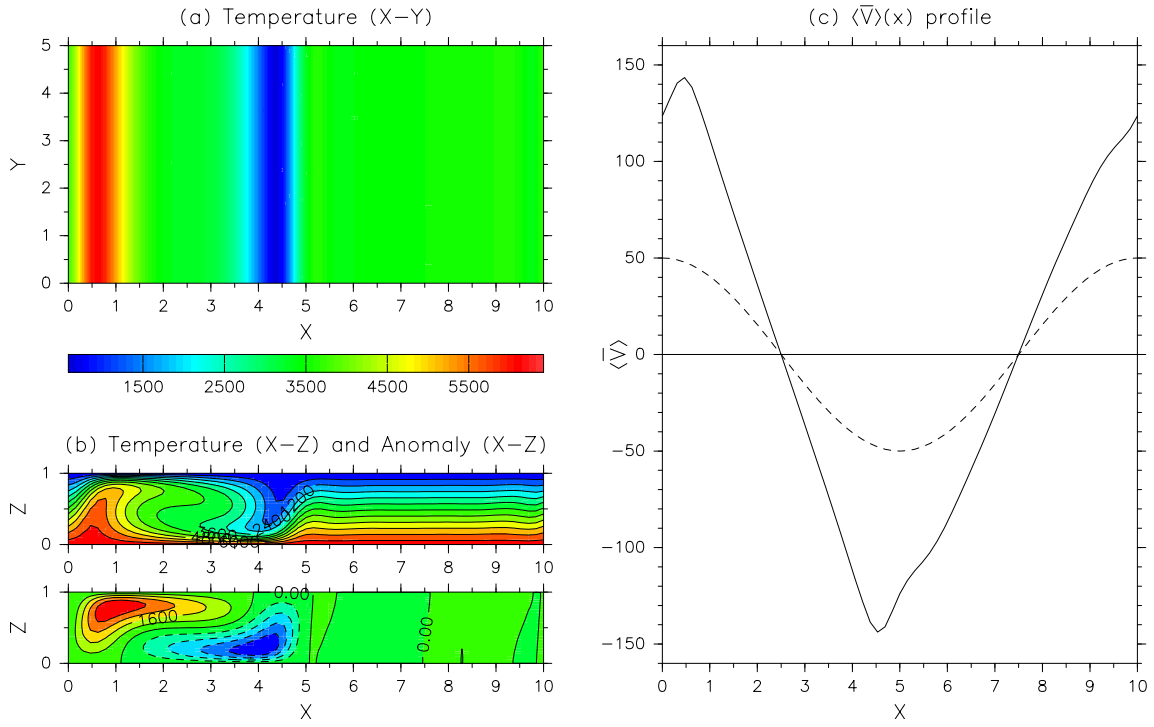


Figure 5. A snapshot of the nonlinear time evolution for the case in which $Ta = 10^4$, $\theta = 45^\circ$, and $Ra = 7,000$ at $t = 10.0$. (a) x - y sectional view of the temperature field at $z = 0.5$. (b) x - z sectional views of the temperature field and its anomaly field at $y = 2.5$. (c) Solid line: zonally and vertically averaged flow profile $\langle \bar{V} \rangle(x)$. Dashed line: $\langle \bar{v} \rangle(x)$ profile at $t = 0.0$.

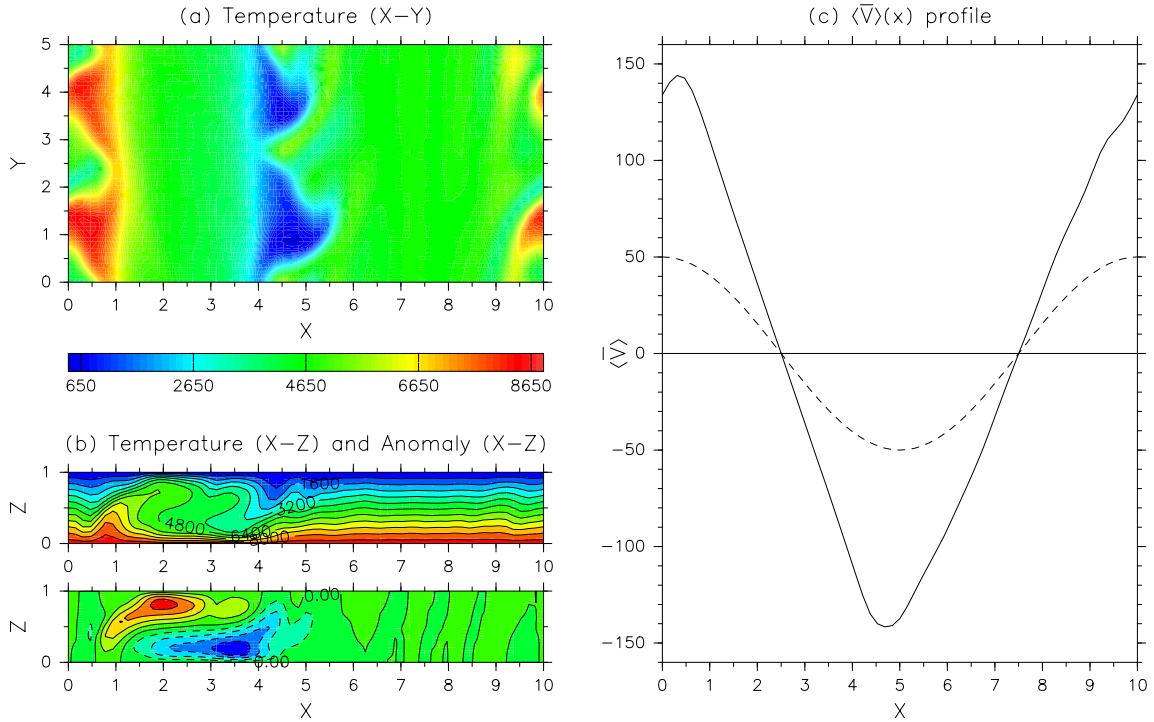


Figure 6. Same as figure 5, except for $Ra = 9,300$.

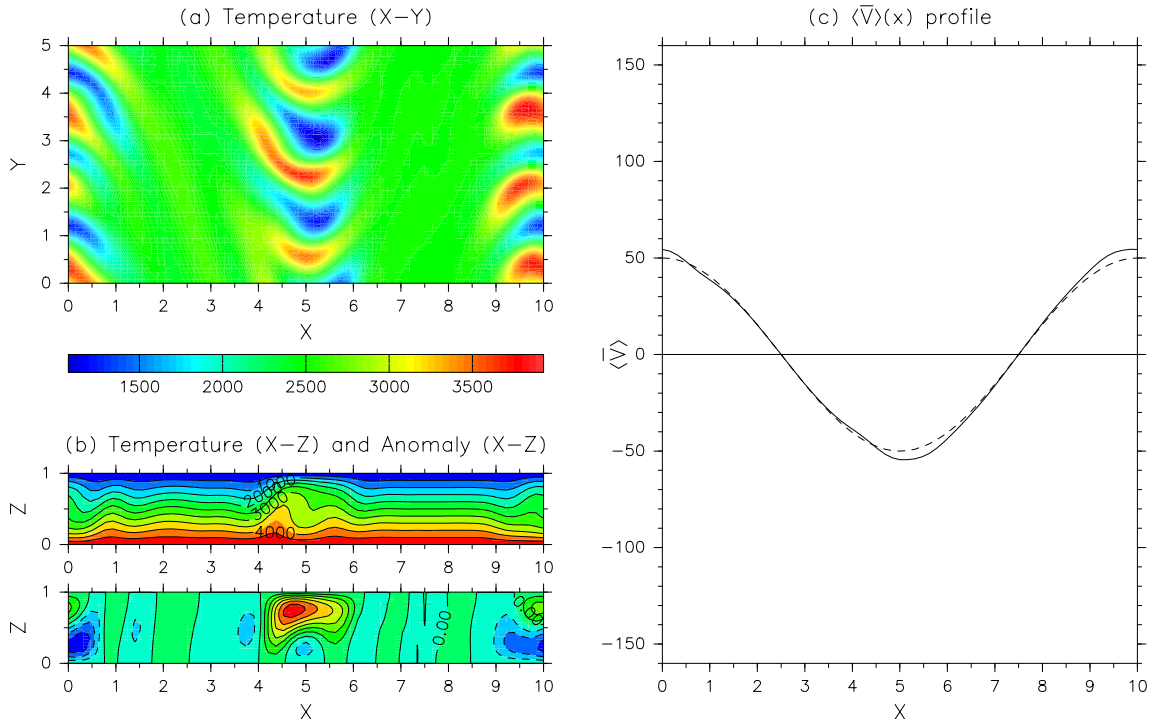


Figure 7. Same as figure 5, except for $\theta = 30^\circ$ and $Ra = 5,000$.

which a herringbone pattern remains in the x - y sectional view of the temperature field (figure 7(a)). Figure 8 shows the final state for $Ta = 10^4$, $\theta = 75^\circ$, and $Ra = 5,000$. In this case, small-scale roll convections parallel to the y axis are observed (figure 8(a)), corresponding to the fact that the system is linearly stable to disturbances of $m \neq 0$ but unstable to disturbances of $m = 0$ (c.f., tables 1 and 2). When Ra is large, the final state becomes turbulent. Figure 9 shows an example of the final turbulent state for $Ta = 10^4$, $\theta = 15^\circ$, and $Ra = 9,500$. Figure 10 shows another example of the final turbulent state for $Ta = 10^4$, $\theta = 75^\circ$, and $Ra = 7,700$. This final turbulent state is regarded as a mixture of roll convections of a herringbone pattern and small-scale roll convections (figure 10(a)). In this case, the system is linearly unstable not only to disturbances of $m = 0$ but also to disturbances of $m \neq 0$ (c.f., tables 1 and 2).

The dependence of the final convection pattern on the experimental parameters is summarized in figure 11 for $Ta = 10^4$. A magnified view of the regime diagram is also shown in figure 12. Here, we classify the final convection patterns into five regimes: 2D large-scale roll (as shown in figure 5), quasi-2D large-scale roll (as shown in figure 6), herringbone pattern (as shown in figure 7), small-scale rolls, including small-scale rolls with weak wavy disturbances (as shown in figure 8), and turbulence (as shown in figures 9 and 10). As shown in figure 11, the (quasi-)2D large-scale roll convection regime, in which the zonal mean flow is accelerated strongly, can be observed for $\theta = 30^\circ$, 45° , and 60° when Ra is relatively large. The formation mechanism of the (quasi-)2D large-scale roll is examined in detail in the next section. On the other hand, herringbone patterns appear for $\theta = 15^\circ$, 30° , 45° , and 60° when Ra is relatively small. This herringbone

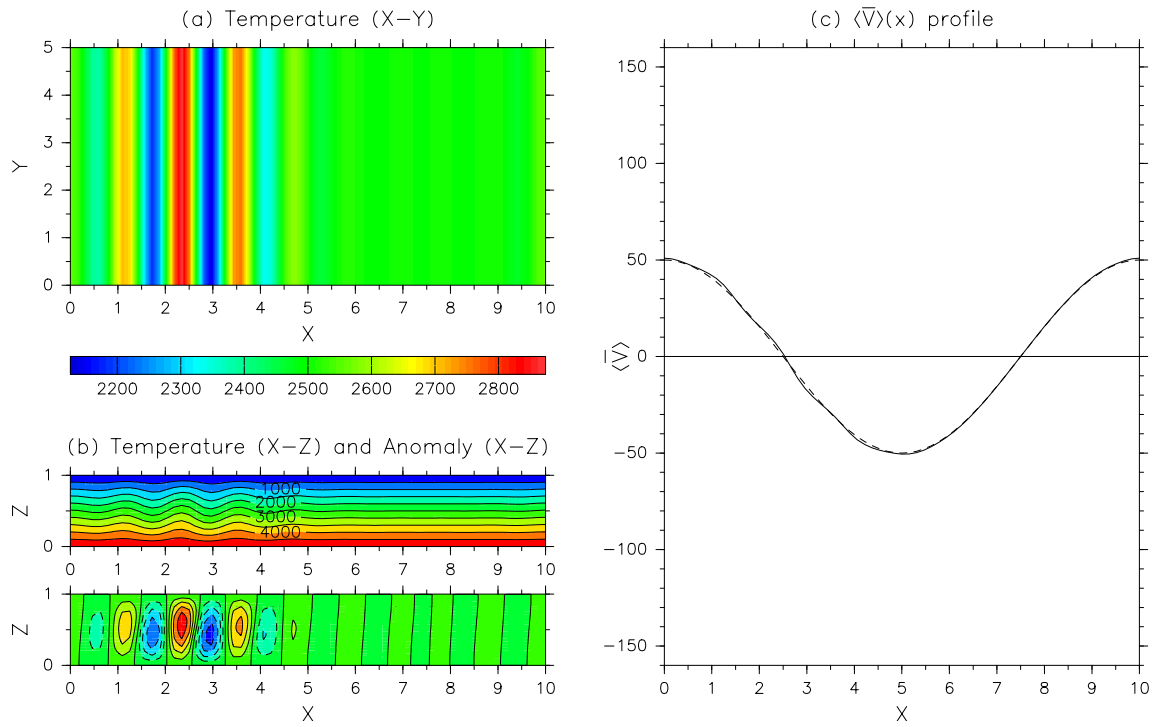


Figure 8. Same as figure 5, except for $\theta = 75^\circ$, $Ra = 5,000$, and $t = 60.0$.

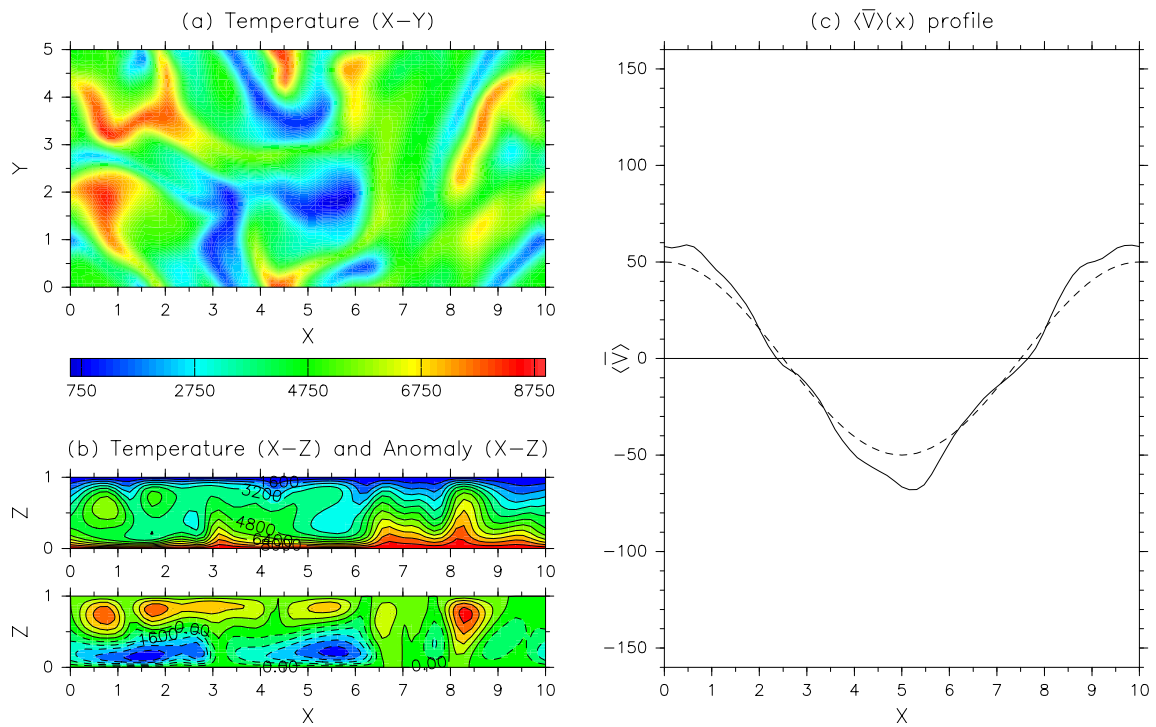


Figure 9. Same as figure 5, except for $\theta = 15^\circ$ and $Ra = 9,500$.

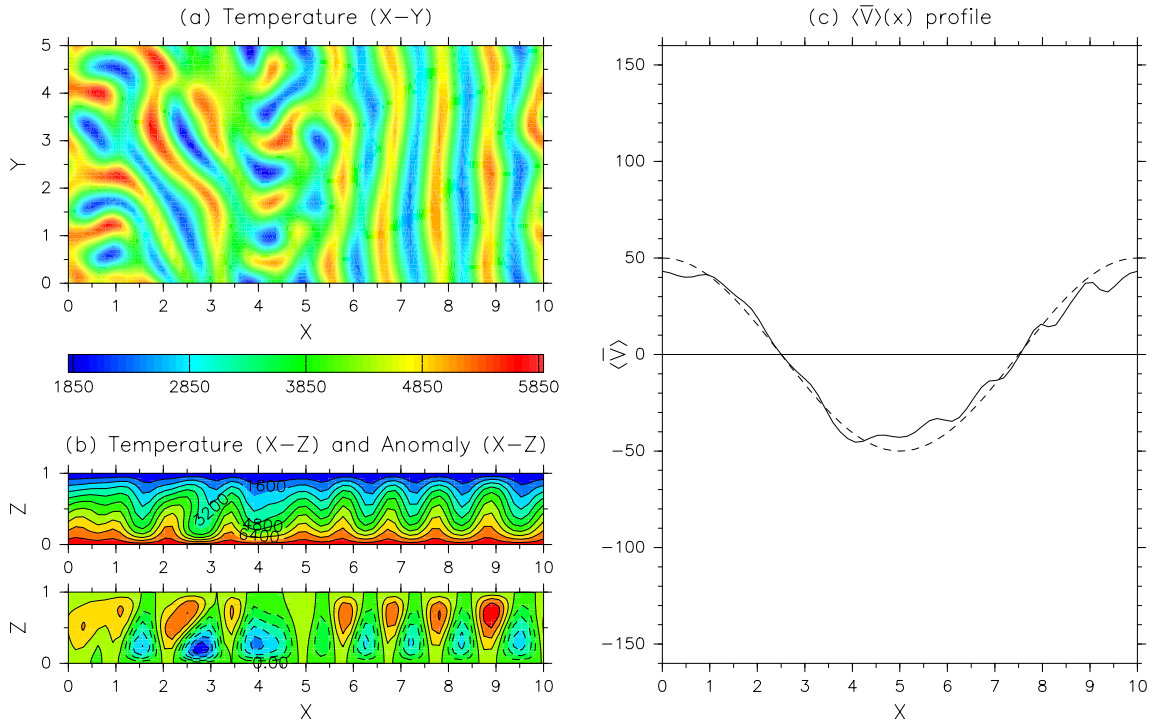


Figure 10. Same as figure 5, except for $\theta = 75^\circ$ and $Ra = 7,700$.

pattern regime was explored deeply by Saito and Ishioka (2009). We present an overview of the results of their study in Appendix C for the convenience of the reader. Here, we determine the border between each regime by observing time evolutions. We can judge whether the flow has a turbulent nature by examining time evolution of vertical profile of the horizontal mean temperature (figure 13). The overwritten line plots coincide for a herringbone pattern regime (figure 13(a)) while those spread for a turbulent regime (figure 13(b)). Note that the regime of quasi-2D large-scale roll convection has a turbulent nature when Ra is large and line plots spread if we draw time evolution of vertical profile of the horizontal mean temperature as figure 13(b) (not shown).

The regime diagram changes depending on the Taylor number. Figure 14 shows the regime diagram for $Ta = 3 \times 10^4$, and figure 15 shows that for $Ta = 10^5$. As Ta is increased, Ra_c increases and each regime found for $Ta = 10^4$, roughly speaking, moves toward the positive direction of the Ra axis. When $Ta = 3 \times 10^4$, the quasi-2D large-scale roll convection regime can be seen for $\theta = 30^\circ$ and 45° . Although we cannot find the large-scale roll convection regime for $Ta = 10^5$ in the parameter range for which we have swept, several additional experiments show that the large-scale roll convection regime exists where $Ra \approx 60,000$ for $\theta = 30^\circ$ and $Ra \approx 70,000$ for $\theta = 45^\circ$ (figures are not shown).

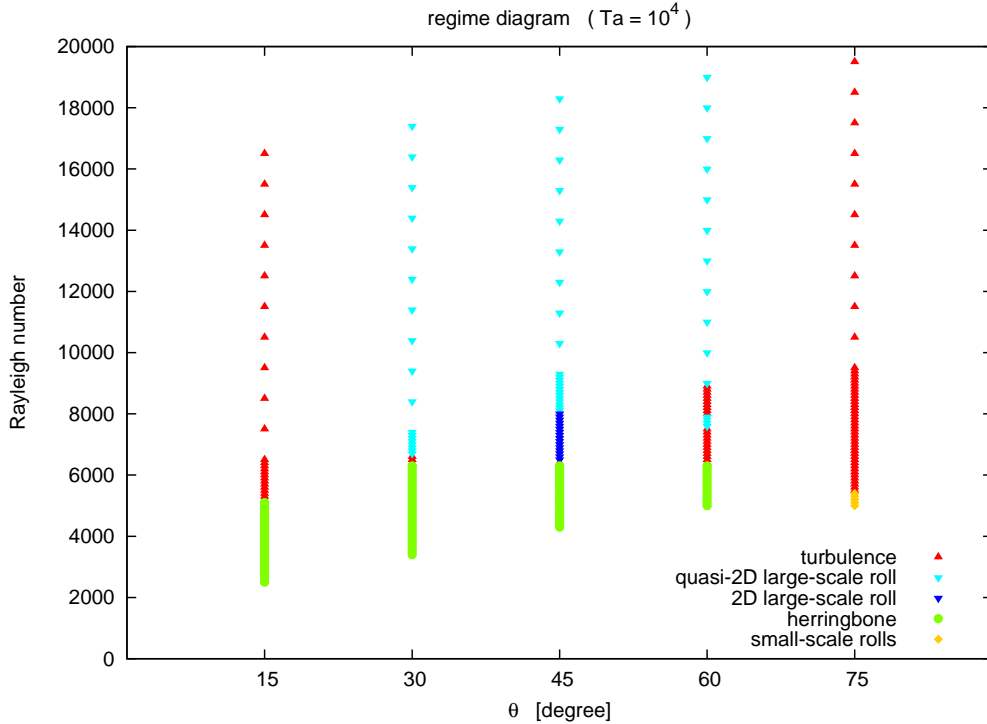


Figure 11. Regime diagram for $Ta = 10^4$. The horizontal axis is the tilt angle of the rotation axis θ , and vertical axis is the Rayleigh number Ra . Red triangles, light blue upside-down triangles, blue upside-down triangles, green circles, and orange diamonds represent turbulent states, regimes of quasi-2D large-scale roll convection, regimes of 2D large-scale roll convection, regimes of roll convection of a herringbone pattern, and regimes of small-scale roll convection, respectively.

4. Analyses of the acceleration of a mean flow by the transition to the regime of a large-scale roll convection

As described in the previous section, the zonal mean flow is strongly accelerated when a large-scale roll convection appears. Therefore, in this section, we explore why such a large-scale roll convection appears and how this convection accelerates the mean flow.

4.1. Search for 2D steady solutions

The large-scale roll convection that appears in the nonlinear time evolution shown in the previous section appears to be a stable steady solution of the system. In the following, we investigate whether perfectly 2D stable steady solutions exist.

We first calculate the nonlinear time evolution of the 2D (x - z) model for $Ta = 10^4$, $\theta = 45^\circ$, and $Ra = 6,500$ until it converges to a steady roll solution. The initial condition is set as the $m = 0$ component of the final state (at $t = 10.0$) of the corresponding 3D nonlinear time evolution, in which a large-scale east–west roll convection is formed. We then calculate the 2D nonlinear time evolution from an initial condition, which is set as the converged solution that we found in the previous calculation, changing the values

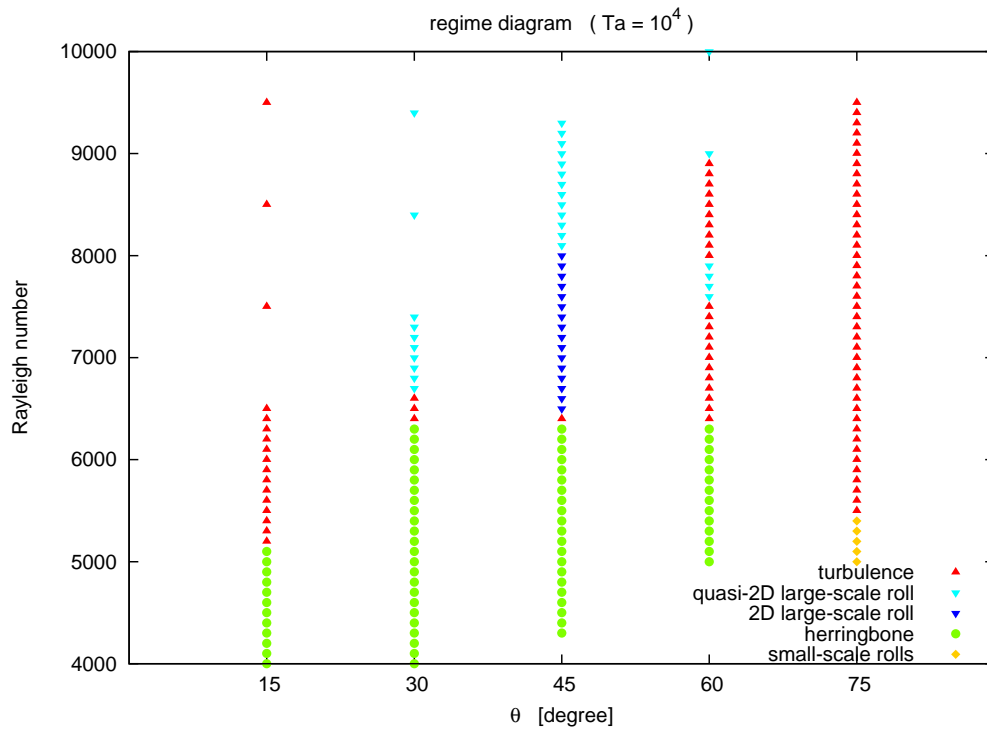


Figure 12. A magnified view of figure 11 for $4,000 \leq Ra \leq 10,000$.

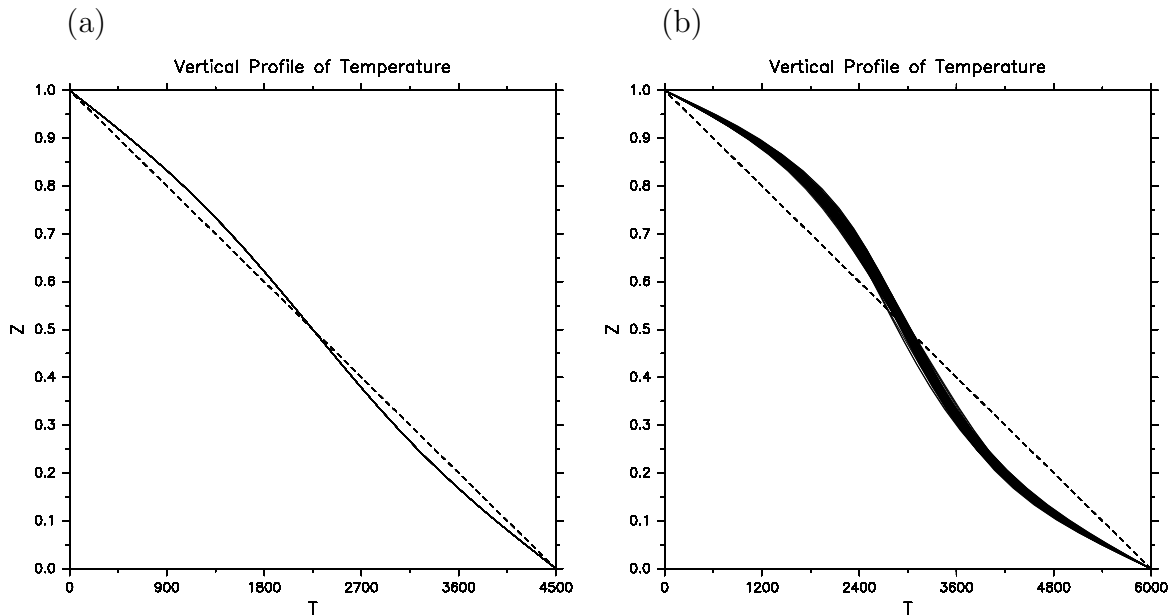


Figure 13. Snapshots of the vertical profile of the horizontal mean temperature for $Ta = 10^4$ and $\theta = 15^\circ$ (solid line). (a) for a herringbone pattern regime ($Ra = 4500$) and (b) for a turbulent regime ($Ra = 6000$). The profiles are drawn on every 0.01 nondimensional time from $t = 8.0$ to 9.0. The horizontal axis is temperature T and the vertical axis is z . Dashed line is the initial profile, which is the heat conduction solution.

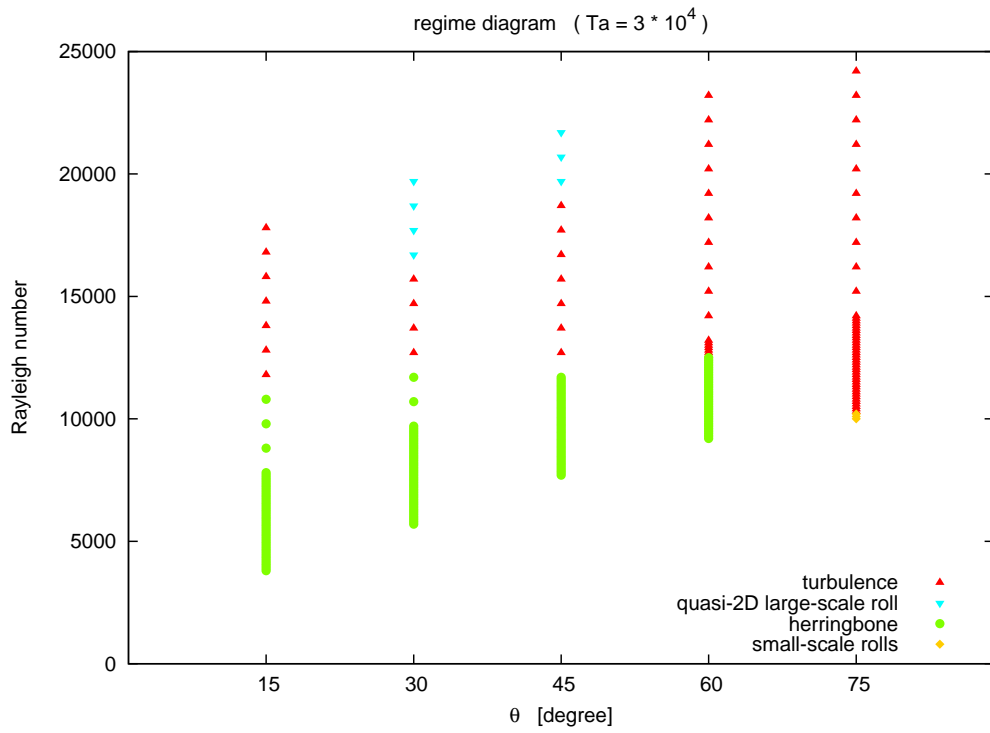


Figure 14. Regime diagram for $Ta = 3 \times 10^4$.

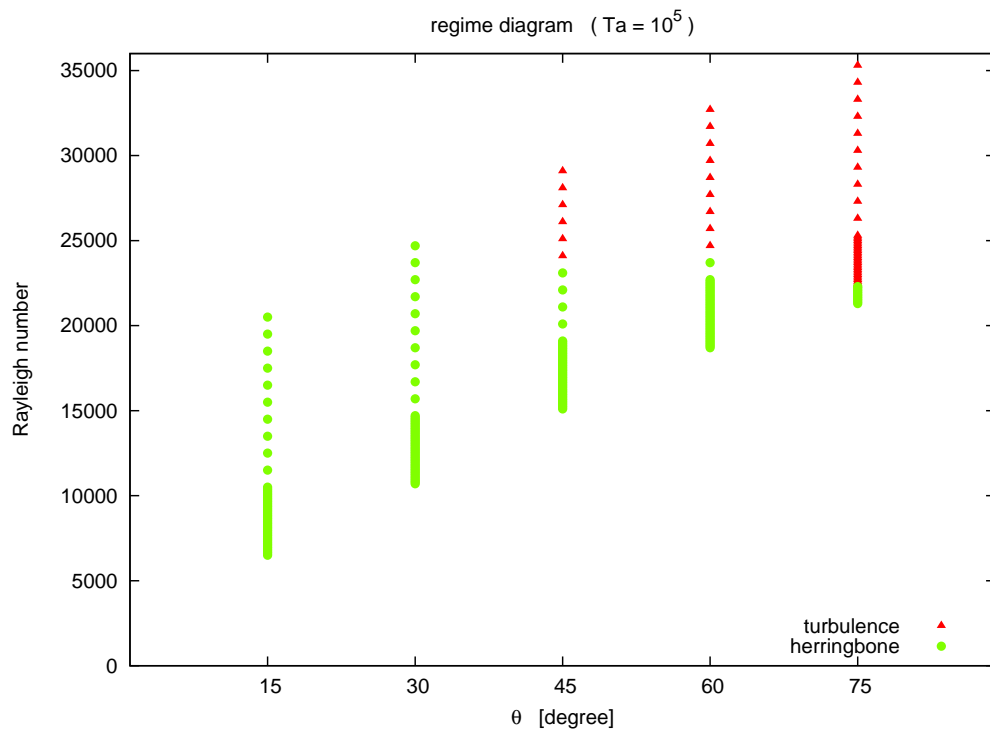


Figure 15. Regime diagram for $Ta = 10^5$.

of Ra and θ . By repeating this procedure, we determine the parameter regime in which a large-scale 2D steady roll solution exists.

The 2D steady solutions, however, are not always stable with respect to 3D disturbances. Next, we perform linear stability analysis of the 2D steady solutions in order to determine whether these solutions are stable to 3D disturbances. Figure 16 shows a regime diagram of stable and unstable 2D steady roll convections for $Ta = 10^4$. A magnified view of the regime diagram is also shown in figure 17. A difference is found between the parameter region in which 2D stable steady solutions exist and the region in which a large-scale east–west roll convection appears in the nonlinear time evolutions (c.f., figure 11 or figure 12). Let us examine the correspondence between the 2D steady solutions and the final states of the 3D nonlinear time evolutions for $Ta = 10^4$ and $\theta = 45^\circ$ in detail. In the range of $5,200 \leq Ra \leq 6,400$, a large-scale east–west roll convection does not appear in the nonlinear time evolution, whereas a 2D stable steady solution exists. This is considered to be because the system cannot reach the steady solution from the initial condition. In the range of $6,500 \leq Ra \leq 8,000$, the nonlinear time evolution converges to the 2D large-scale steady roll solution. In the range of $8,100 \leq Ra \leq 9,200$, there still exists a stable 2D steady solution. Although a large-scale east–west roll convection is formed in the nonlinear time evolution, disturbances of wavenumber 2 or 3 do not disappear. It is thought that the disturbances in the final state with respect to the perfectly 2D steady stable solution are so large that the flow pattern settles down to an unsteady quasi-periodic solution oscillating around the steady solution. In the range of $Ra \geq 9,300$, a large-scale east–west roll convection with disturbances of wavenumber 2 or 3 is formed in the nonlinear time evolution, whereas the 2D large-scale steady solution is unstable. It is thought that a transition of the flow pattern to a quasi-periodic solution oscillating around the unstable steady solution occurs. In fact, the largest and second largest growing wavenumbers of the unstable steady solution for $Ra = 10,300$ are 2 and 3, respectively, which is consistent with the wavenumbers of the disturbances in the final state of the nonlinear time evolution.

In summary, when the nonlinear time evolution converges to a perfectly 2D large-scale roll solution, this solution is the stable 2D steady solution of the system. However, whether a 2D stable solution exists does not directly correspond to whether a large-scale roll convection appears in the nonlinear time evolutions.

While the above description is for $\theta = 45^\circ$, let us examine the case in which $\theta = 60^\circ$. Comparing figures 11 and 16 (or the corresponding magnified views in figures 12 and 17, respectively), a 2D stable steady solution exists when $3,800 \leq Ra \leq 6,100$. However, in this range of Ra , the nonlinear time evolution does not converge to a large-scale roll solution. On the other hand, a large-scale roll convection with wavy disturbances appears in the nonlinear time evolution for $7,600 \leq Ra \leq 7,900$ and $Ra \geq 9,000$, even though the 2D steady solution is unstable. This is also the case in the range of $Ra \geq 6,700$ for $\theta = 30^\circ$. Therefore, for some ranges of experimental parameters, the 2D steady roll solution is important in describing a large-scale roll convection that appears in the nonlinear time evolution, even when the steady solution is unstable.

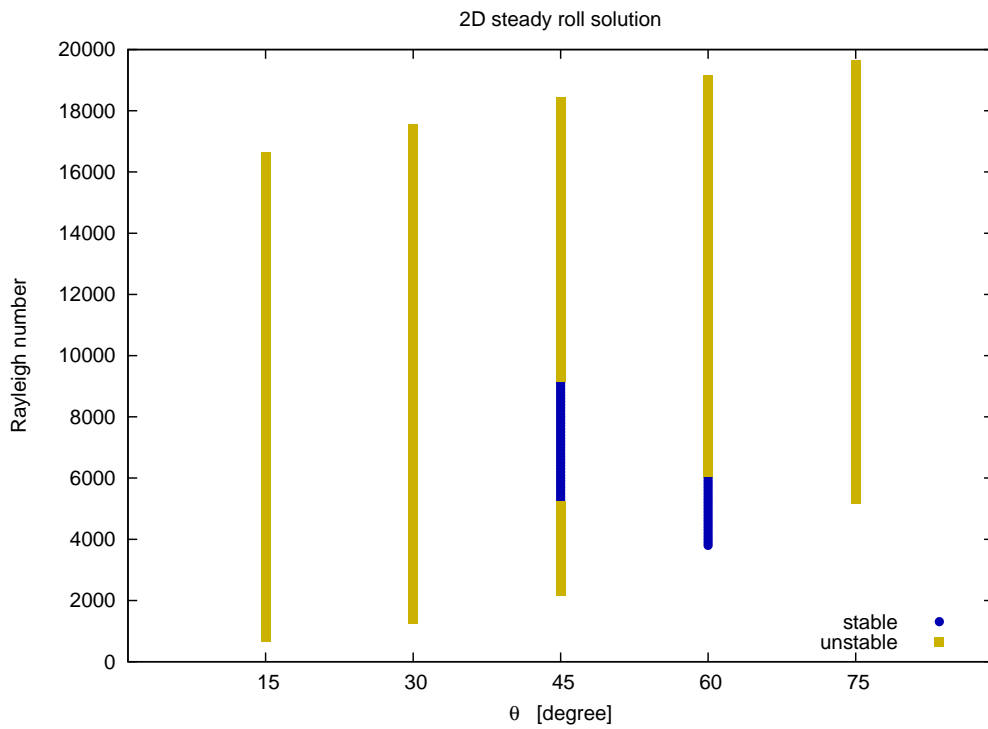


Figure 16. Regime diagram of the stable and unstable 2D steady roll solutions for $Ta = 10^4$. The horizontal axis is the tilt angle, θ , and the vertical axis is the Rayleigh number. Blue circles represent stable solutions, and yellow squares represent unstable solutions.

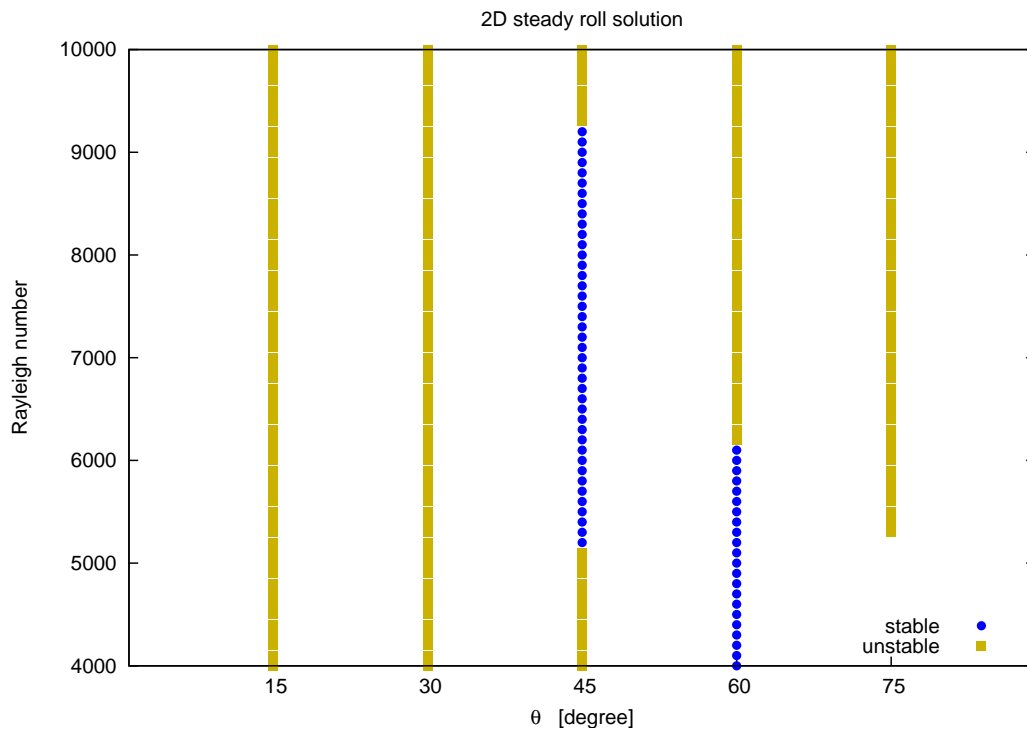


Figure 17. A magnified view of figure 16 for $4,000 \leq Ra \leq 10,000$.

4.2. Explanation of the acceleration mechanism

Now, let us examine how the large-scale roll convection accelerates the zonal mean flow. Considering the tilt of the rotation vector and the horizontal shear of the zonal flow, the acceleration mechanism by a large-scale east–west roll convection is explained as follows:

- (i) The region of $0 < x < 5$ is convectively more unstable than that of $5 < x < 10$ because the horizontal shear of the zonal flow has the opposite sign to the vertical component of the system rotation in the region of $0 < x < 5$. On the other hand, the opposite occurs in the region of $5 < x < 10$, which leads to a reduction in convective instability.
- (ii) Let us assume that a large-scale roll convection is formed in the region of $0 < x < 5$ with an upward flow near $x = 0.5$ and a downward flow near $x = 4.5$ (figure 18(a)).
- (iii) The Coriolis force acting on the upward and downward flows accelerates the mean flow westward and eastward, respectively, which enhances the horizontal shear of the zonal flow (figure 18(b)). Here, the horizontal component of the system rotation plays an important roll.
- (iv) The enhanced horizontal shear further destabilizes the region of $0 < x < 5$, so that the large-scale east–west roll convection is enhanced. In contrast, the region of $5 < x < 10$ is stabilized. The positive feedback in the region of $0 < x < 5$ occurs because we are assuming an upward flow near $x = 0.5$ and a downward flow near $x = 4.5$. If we assume the opposite vertical flow pattern, the feedback becomes negative.
- (v) As the convection becomes intense, horizontal transport of the zonal momentum by the overturning flow grows to have a tendency to decelerate the zonal flow. The entire flow pattern becomes steady when the acceleration by the Coriolis force and the deceleration by the horizontal transport of the zonal momentum balance. Figure 19 shows the balance in the final state for $Ta = 10^4$, $\theta = 45^\circ$, and $Ra = 7,000$. (The equation of $\partial\langle\bar{v}\rangle/\partial t$ and the definition of each effect drawn in the figure 19 are shown in Appendix D.)

Thus, the acceleration mechanism described above can work only in a system with a tilted rotation axis and a sine-type horizontal shear flow.

5. Summary and discussion

In the present paper, we investigated thermal convection in a sine-type horizontal shear flow in a rotating system with a tilted axis, sweeping three parameters: the Taylor number, the tilt angle of the rotation axis (i.e., latitude), and the Rayleigh number. Nonlinear time evolutions have shown that there exists not only a regime in which roll convections of a herringbone pattern accelerate the mean flow but also a regime in which a large-scale east–west roll convection accelerates the mean flow strongly. By

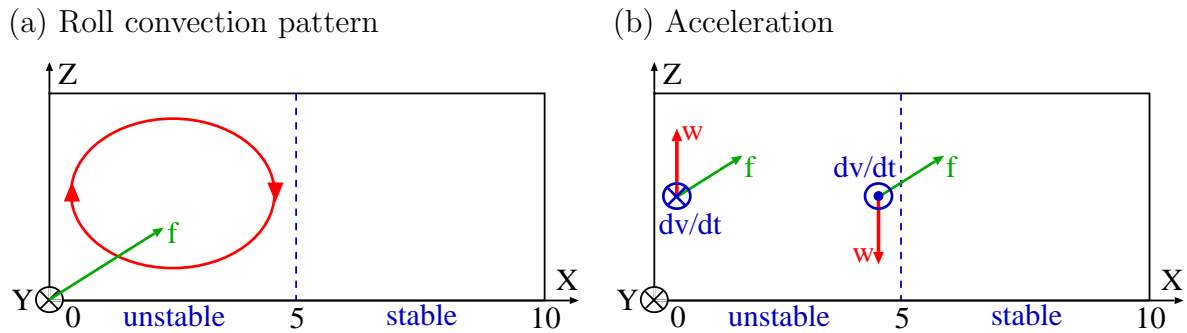


Figure 18. Schematic diagram of the acceleration mechanism of the mean flow by a large-scale east–west roll convection. Green arrows represent rotation vectors. (a) Roll convection pattern. The red oval represents the overturning flow pattern of a large-scale east–west roll convection. (b) Acceleration. Red arrows represent the vertical flow associated with the roll convection. Blue circles represent the direction of the acceleration of the mean flow by the Coriolis force acting on the vertical flow. The cross symbol indicates the westward direction, whereas the dot symbol indicates the eastward direction.

means of 2D calculations and linear stability analyses, it has been demonstrated that stable/unstable steady 2D roll solutions exist. The appearance of the large-scale roll convections in the nonlinear time evolutions can be regarded as a transition to the stable 2D solution or a quasi-periodic solution around the steady solution.

The occurrence of the transition and the acceleration of the zonal flow by the large-scale roll convection are accounted for by the following feedback mechanism. The region in which the horizontal shear of the zonal flow has the opposite sign to the vertical component of the system rotation is convectively more unstable than the region without the shear flow. Once a large-scale roll convection rising in the westward mean flow and descending in the eastward mean flow is formed in the aforementioned region, the Coriolis force acting on the upward and downward flows accelerates the mean flow westward and eastward, respectively, which enhances the horizontal shear of the zonal flow. The enhanced horizontal shear further destabilizes this region so that the large-scale east–west roll convection is enhanced.

Not only a tilted rotation axis but also a sine-type horizontal shear flow is necessary for this feedback mechanism to work. Most of previous studies on thermal convection in a tilted f -plane have not found this feedback mechanism because they have not included such a basic flow. Although Hathaway and Somerville (1987) included a sine-type horizontal shear flow, they did not find the feedback mechanism, either, within the relatively narrow parameter region for which they swept.

The validity of imposing such a basic zonal flow, however, should be discussed. As Hathaway and Somerville (1987) described, we assume that there is some effect, such as the Rhines effect of β -plane turbulence (Rhines 1975), that maintains the zonal flow. In the future, we intend to investigate whether a spontaneously formed zonal flow by the Rhines effect can be accelerated through the feedback mechanism we found in the

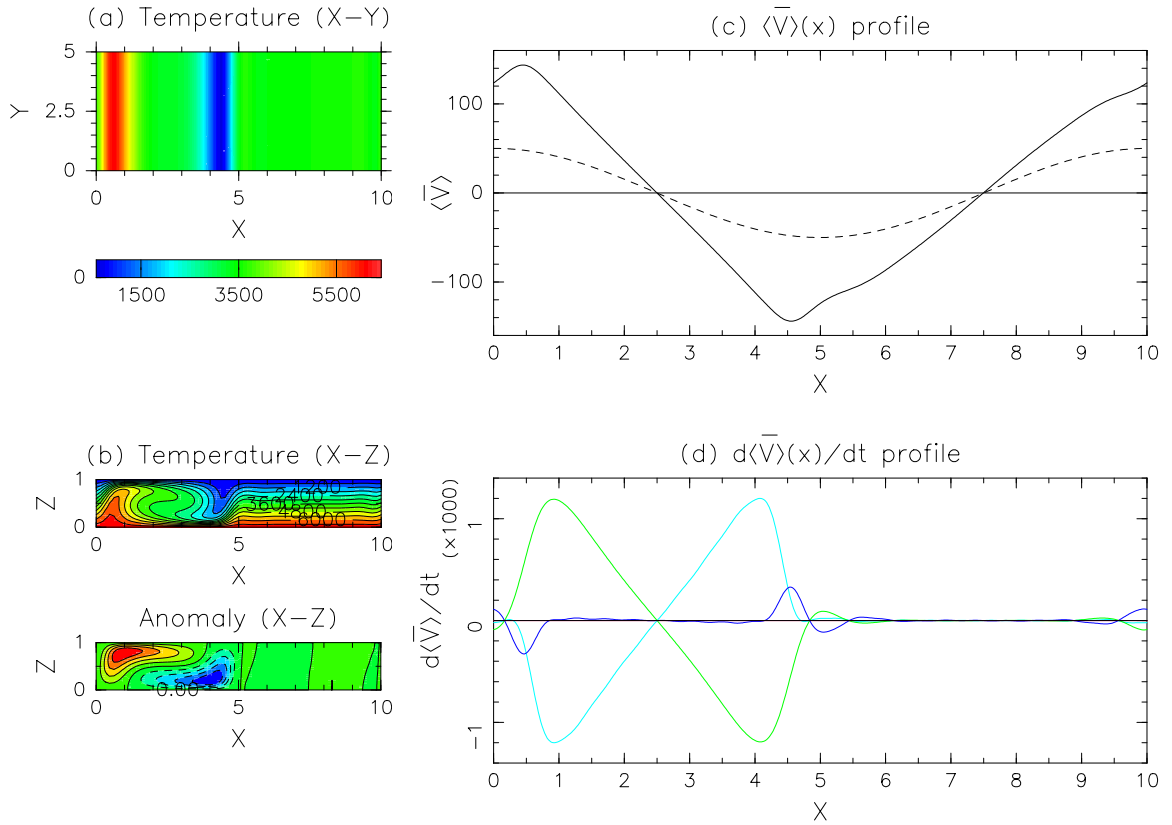


Figure 19. A snapshot of the nonlinear time evolution for the case in which $Ta = 10^4$, $\theta = 45^\circ$, and $Ra = 7,000$ at $t = 10.0$. (a), (b), and (c) are the same as figure 5. (d) The profiles of the accelerations in the zonal (y) direction by the following effects of the roll convection. The green line represents the effect of the Coriolis force acting on the vertical flow. The light blue line represents the effect of the horizontal transport of the zonal momentum by the overturning flow. The blue line represents the effect of viscosity. The summation of the aforementioned three effects is zero because the flow has settled to a steady state.

present study, by including the β effect in the system.

As for the relevance of this study to the real planetary atmospheres, one may suspect that the strong mean flow acceleration found in this study is worthless since the strong acceleration occurs not in the turbulent regime but in the quasi-2D large-scale roll convection regime. Although we classified the regime in which the mean flow is significantly accelerated as the regime of “quasi-2D large-scale roll convection”, the flow field in the regime has a turbulent nature when Ra is large. We think the regime of *turbulent* quasi-2D large-scale roll convection may have some relevance to the real planetary atmospheres like Jupiter even though Ra for the real planetary atmospheres is much larger than that examined in this study. In order to examine this speculation, a wider experimental parameter range should be explored in the future.

Acknowledgments

Naoaki Saito was supported by the Ministry of Education, Culture, Sports, Science and Technology of Japan through a Grant-in-Aid for JSPS Fellows, 21-57051, 2009.

Appendix A. Spectral expansion of dependent variables

We use the Legendre polynomials for spectral expansion in the vertical direction. The Legendre polynomials are defined as follows:

$$P_n(\mu) = \sqrt{2n+1} \frac{1}{2^n n!} \frac{d^n}{d\mu^n} (\mu^2 - 1)^n \quad (-1 \leq \mu \leq 1, n \geq 0). \quad (\text{A.1})$$

The Legendre polynomials satisfy the following orthogonal relation:

$$\langle P_n(\mu) P_{n'}(\mu) \rangle = \delta_{nn'}. \quad (\text{A.2})$$

Here,

$$\langle \rangle = \frac{1}{2} \int_{-1}^1 d\mu.$$

A variable having a value that vanishes at both ends is expanded as follows:

$$w(z) = \sum_{n=1}^N \hat{w}_n \phi_n(z) \quad (-1 \leq z \leq 1). \quad (\text{A.3})$$

Here, $\phi_n(z)$ ($n = 1, 2, \dots, N$) are defined as follows:

$$\begin{aligned} \phi_n(z) &\equiv \int_{-1}^z P_n(\mu) d\mu \\ &= \frac{P_{n+1}(z)}{\sqrt{(2n+1)(2n+3)}} - \frac{P_{n-1}(z)}{\sqrt{(2n-1)(2n+1)}} \end{aligned} \quad (\text{A.4})$$

and satisfy the following relations:

$$\frac{d\phi_n(z)}{dz} = P_n(z), \quad \phi_n(\pm 1) = 0. \quad (\text{A.5})$$

A variable having a z -derivative that vanishes at both ends is expanded as follows:

$$v(z) = \sum_{n=0}^N \hat{v}_n \xi_n(z) \quad (-1 \leq z \leq 1). \quad (\text{A.6})$$

Here,

$$\xi_0 = 1, \quad (\text{A.7})$$

$$\xi_n(z) = \int_{-1}^z \phi_n(z') dz' - \left\langle \int_{-1}^z \phi_n(z') dz' \right\rangle \quad (n = 1, 2, \dots, N), \quad (\text{A.8})$$

which satisfy the following relations:

$$\langle \xi_n(z) \rangle = 0 \quad (n \geq 1), \quad \frac{d\xi_n}{dz}(\pm 1) = 0. \quad (\text{A.9})$$

The dependent variables are expanded as follows:

$$u(x, y, z) = \sum_{l=-L}^L \sum_{m=-M}^M \sum_{n=0}^N \hat{u}_{lmn} e^{i(r_x l x + r_y m y)} \xi_n(z), \quad (\text{A.10})$$

$$v(x, y, z) = \sum_{l=-L}^L \sum_{m=-M}^M \sum_{n=0}^N \hat{v}_{lmn} e^{i(r_x l x + r_y m y)} \xi_n(z), \quad (\text{A.11})$$

$$w(x, y, z) = \sum_{l=-L}^L \sum_{m=-M}^M \sum_{n=1}^N \hat{w}_{lmn} e^{i(r_x l x + r_y m y)} \phi_n(z), \quad (\text{A.12})$$

$$b(x, y, z) = \sum_{l=-L}^L \sum_{m=-M}^M \sum_{n=1}^N \hat{b}_{lmn} e^{i(r_x l x + r_y m y)} \phi_n(z), \quad (\text{A.13})$$

$$\omega_1(x, y, z) = \sum_{l=-L}^L \sum_{m=-M}^M \sum_{n=1}^N (\hat{\omega}_1)_{lmn} e^{i(r_x l x + r_y m y)} \phi_n(z), \quad (\text{A.14})$$

$$\omega_2(x, y, z) = \sum_{l=-L}^L \sum_{m=-M}^M \sum_{n=1}^N (\hat{\omega}_2)_{lmn} e^{i(r_x l x + r_y m y)} \phi_n(z), \quad (\text{A.15})$$

$$\omega_3(x, y, z) = \sum_{l=-L}^L \sum_{m=-M}^M \sum_{n=0}^N (\hat{\omega}_3)_{lmn} e^{i(r_x l x + r_y m y)} \xi_n(z), \quad (\text{A.16})$$

where $r_x = 2\pi/L_x$, $r_y = 2\pi/L_y$, L is the truncation wavenumber in the x direction, and M is that in the y direction.

Appendix B. The relevance of the chosen values of V_0 and Ta compared with the Jupiter atmosphere

As explained in section 4, in order for the large-scale zonal convection regime to appear, the value of ζ must be of the same order as f_z . Here, ζ is the maximum value of the horizontal shear and $f_z = f \sin \theta$. Table B1 compares ζ , f_z , and ζ/f_z at $\theta = 30^\circ$ for $Ta = 10^4$ and $Ta = 10^5$ in the experiments of this paper with those of the Jupiter atmosphere near 25°N from Cassini data. From this table, we do not think the parameter region we explore is unrealistic as for the value of ζ/f_z .

Table B1. Comparison of the typical value of ζ/f_z used in this paper ($Ta = 10^4$, 10^5 , and $\theta = 30^\circ$) with that of the Jupiter atmosphere (near 25°N).

| | $\zeta (= \partial v / \partial x)$ | f_z | ζ / f_z |
|-------------|--|-----------------------------------|--|
| $Ta = 10^4$ | $2\pi V_0 / L_x = 31.4$ | $\sqrt{10^4} \sin 30^\circ = 50$ | $31.4 / 50 = 1 / 1.59$ |
| $Ta = 10^5$ | | $\sqrt{10^5} \sin 30^\circ = 158$ | $31.4 / 158 = 1 / 5.03$ |
| Jupiter | $130[\text{m/s}] / (4 \times 10^6)[\text{m}]$ $= 3.2 \times 10^{-5} [1/\text{s}]$ | $1.5 \times 10^{-4} [1/\text{s}]$ | $(3.2 \times 10^{-5}) / (1.5 \times 10^{-4})$ $= 1 / 4.7$ |

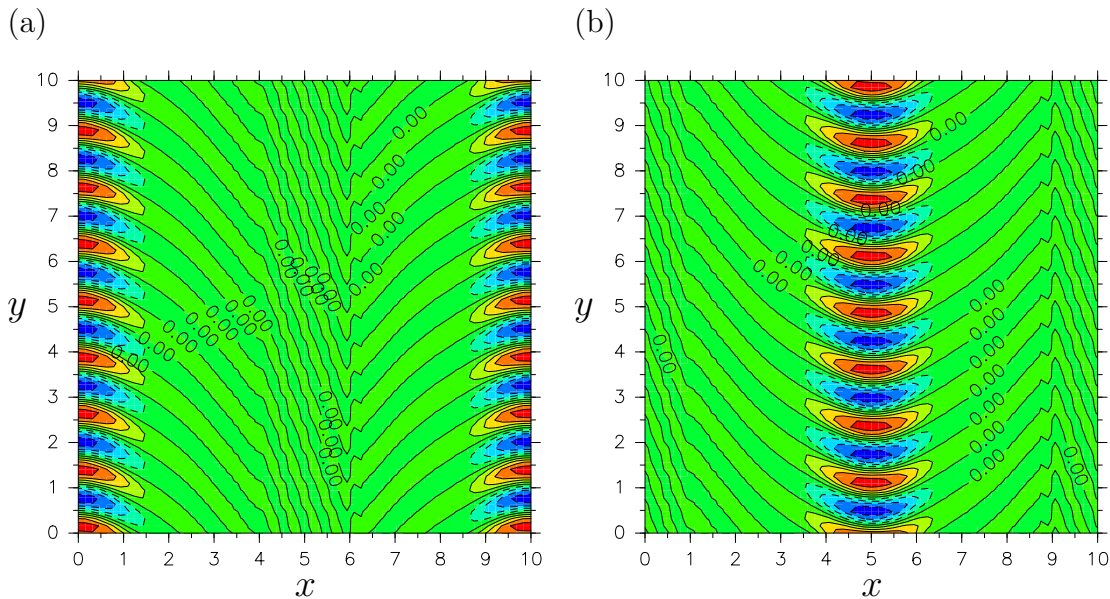


Figure C1. x - y sectional views of the temperature field of the two largest growing eigenmodes for the case in which $Ta = 10^5$, $\theta = 15^\circ$, and $Ra = 10^4$, that have the same growth rate and the structure of a herringbone pattern. (a) Eigenmode that has a peak at $x = 0$. (b) Eigenmode that has a peak at $x = 5$. This figure is taken from Saito and Ishioka (2009).

Appendix C. Acceleration of the mean flow by roll convection of a herringbone pattern

The regime in which roll convections of a herringbone pattern accelerate the mean flow was investigated in detail by Saito and Ishioka (2009). In this appendix, we summarize their results briefly for the convenience of the reader. Their model settings are almost the same as those used in the present paper, except that L_x is set to 10 and the experimental parameters are limited to $Ra = 10^4$, $\theta = 15^\circ$, and $Ta = 0, 10^4, 3 \times 10^4$, and 10^5 .

Linear stability analyses of the basic state in the cases of $Ta = 3 \times 10^4$ and $Ta = 10^5$, in which roll convections of a herringbone pattern are formed in the nonlinear time evolutions, are performed. Figure C1 shows x - y sectional views of the temperature field of the two largest growing eigenmodes for the case in which $Ta = 10^5$. These two eigenmodes have the same growth rate, the same wavenumber in the y direction, and the same structure of a herringbone pattern with a peak at $x = 0$ and $x = 5$, respectively. Roll convections of the herringbone pattern observed in the nonlinear time evolutions correspond to the structure of the fastest growing eigenmodes.

In the nonlinear time evolutions in which a herringbone pattern appears, the growth rate of the deviation of the mean flow velocity from the initial velocity v_B is twice as large as the largest growth rate of linear eigenmodes. This implies that the acceleration of the mean flow is due to the second-order effect of the fastest growing eigenmode.

In order to examine which effect contributes most to the acceleration, the second-

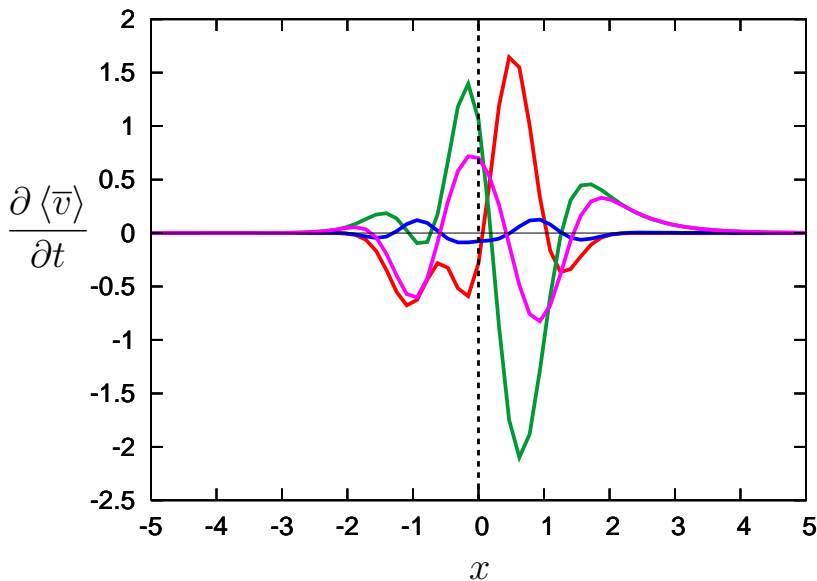


Figure C2. Acceleration profiles by the second-order effects of the eigenmode with a peak at $x = 0$ for the case in which $Ta = 3 \times 10^4$, $\theta = 15^\circ$, and $Ra = 10^4$. The red line represents the effect of direct momentum transport. The green line represents the effect of the Coriolis force acting on the second-order vertical flow. The blue line represents the effect of viscosity. The purple line represents the sum of the three effects, i.e., the net acceleration. This figure is taken from Saito and Ishioka (2009).

order acceleration by the eigenmode is decomposed. Figure C2 shows the acceleration profiles given by three effects of the eigenmode for the case in which $Ta = 3 \times 10^4$. These three effects are direct momentum transport, the Coriolis force acting on the second-order vertical flow, and viscosity. Comparing these three effects reveals that the Coriolis force acting on the second-order vertical flow contributes to the net acceleration more than direct momentum transport.

Based on further detailed analyses, the mechanism of the acceleration of the mean flow by the second-order effect of the fastest growing eigenmode with a peak at $x = 0$ is described as follows. A schematic diagram of the following description is shown in figure C3. For the fastest growing eigenmode with a peak at $x = 5$, the direction of the acceleration is reversed.

- (i) Roll convection localizes around $x = 0$, where the horizontal shear of the mean flow is weak. The axis of each roll convection tilts parallel to the rotation vector \mathbf{f} . The overturning flow of roll convection is faster in $0 < x < 5$ than in $-5 < x < 0$ because the former region is convectively more unstable than the latter region.
- (ii) Heat transport by the roll convections generates buoyancy deviations. The absolute value of the upper positive buoyancy deviation is larger than that of the lower negative buoyancy deviation, corresponding to the localization, the axis tilt, and the strength asymmetry of the roll convections described in (i).
- (iii) The vertical mean of the buoyancy deviation near $x = 0$ becomes positive, which

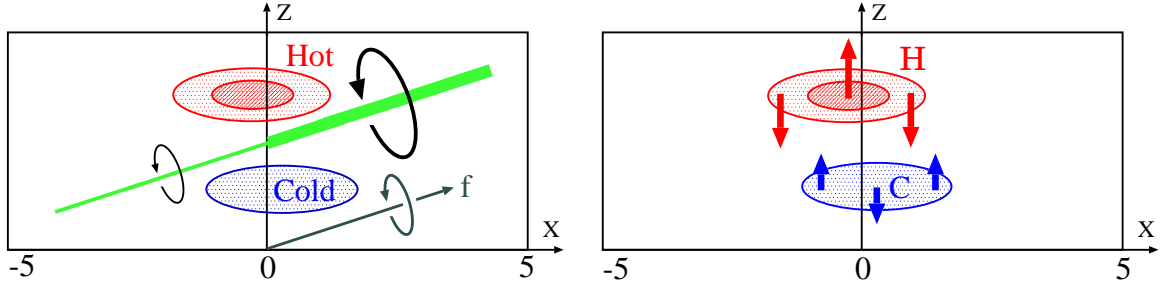


Figure C3. Schematic diagram of the acceleration of the mean flow by roll convections of a herringbone pattern. The green line represents the axis of each convection roll. The red and blue ovals represent positive and negative buoyancy deviations, respectively. The red and blue arrows represent the second-order vertical flow. This figure is taken from Saito and Ishioka (2009).

induces upward second-order vertical flow.

- (iv) The Coriolis force acting on the upward flow accelerates the mean flow. The horizontal component of \mathbf{f} is important for the acceleration.

Appendix D. Derivation of the equation that describes time evolution of the mean flow

In this appendix, we derive the equation that describes time evolution of the mean flow in order to examine which effect contributes to the acceleration.

The equation of motion (2.1) can be rewritten as

$$\frac{\partial \mathbf{u}}{\partial t} + \frac{1}{2} \nabla |\mathbf{u}|^2 = \mathbf{u} \times \boldsymbol{\omega} - \nabla p - \mathbf{f} \times (\mathbf{u} - \mathbf{u}_B) + Ra \mathbf{b} + \nabla^2 (\mathbf{u} - \mathbf{u}_B). \quad (\text{D.1})$$

Taking the y component of (D.1) yields

$$\frac{\partial v}{\partial t} + \frac{1}{2} \frac{\partial}{\partial y} |\mathbf{u}|^2 = (w \omega_1 - u \omega_3) - \frac{\partial p}{\partial y} - (f_3 u - f_1 w) + \nabla^2 (v - v_B). \quad (\text{D.2})$$

Here, f_1 and f_3 are the x and the z components of the rotation vector, respectively. Averaging (D.2) in the y direction and using the periodic boundary condition, we obtain

$$\frac{\partial \bar{v}}{\partial t} = \overline{(w \omega_1 - u \omega_3)} - f_3 \bar{u} + f_1 \bar{w} + \left(\frac{\partial^2}{\partial x^2} + \frac{\partial^2}{\partial z^2} \right) (\bar{v} - v_B). \quad (\text{D.3})$$

Here the overbar ($\bar{\quad}$) indicates the average in the y direction. Averaging (D.3) in the z direction and using the boundary conditions at the top and the bottom, we obtain

$$\frac{\partial \langle \bar{v} \rangle}{\partial t} = \langle \overline{w \omega_1 - u \omega_3} \rangle + f_1 \langle \bar{w} \rangle + \frac{\partial^2}{\partial x^2} (\langle \bar{v} \rangle - v_B). \quad (\text{D.4})$$

Here, the bra-ket $\langle \quad \rangle$ indicates the average in the z direction. In (D.4), the term $f_3 \langle \bar{u} \rangle$ does not appear because $\langle \bar{u} \rangle = 0$ in the settings of the model. We decompose the dependent variables in (D.4) as follows:

$$u = \bar{u} + u', \quad w = \bar{w} + w', \quad \omega_1 = \bar{\omega}_1 + \omega'_1, \quad \omega_3 = \bar{\omega}_3 + \omega'_3, \quad (\text{D.5})$$

where the prime (') indicates the deviation from the average in the y direction. Substituting (D.5) into (D.4), we obtain the following equation:

$$\frac{\partial \langle \bar{v} \rangle}{\partial t} = \langle w' \omega'_1 - u' \omega'_3 \rangle + \langle \bar{w} \bar{\omega}_1 - \bar{u} \bar{\omega}_3 \rangle + f_1 \langle \bar{w} \rangle + \frac{\partial^2}{\partial x^2} (\langle \bar{v} \rangle - v_B). \quad (\text{D.6})$$

Here, the first term in the right-hand side is the effect of the eddy momentum transport, the second term is the effect of the horizontal transport of the zonal momentum by the overturning flow, the third term is the effect of the Coriolis force acting on the vertical flow, and the fourth term is the effect of the viscosity. In figure 19, we compare the values of the terms in the right-hand side of (D.6) and we examine which term contributes most to the acceleration of the mean flow. Note that the first term in the right-hand side of (D.6) is so small that it is omitted in figure 19.

References

- Asai T 1970 Three-dimensional features of thermal convection in a plane Couette flow *J. Meteor. Soc. Japan* **48** 18-29
- Chandrasekhar S 1961 *Hydrodynamic and Hydromagnetic Stability* (Oxford: Oxford University Press.) p 134
- Davies-Jones R 1971 Thermal convection in a horizontal plane Couette flow *J. Fluid Mech.* **49** 193-205
- Furukawa Y and Niino H 2006 Study on interaction between a horizontal shear flow and thermal convections *Reports of RIAM Symposium* **17ME-S4** 121-133
- Hathaway D and Somerville R 1983 Three-dimensional simulations of convection in layers with tilted rotation vectors *J. Fluid Mech.* **126** 75-89
- Hathaway D and Somerville R 1987 Thermal convection in a rotating shear flow *Geophys. Astrophys. Fluid Dyn.* **38** 43-68
- Julien K and Knobloch E 1998 Strongly nonlinear convection cells in a rapidly rotating fluid layer: the tilted f -plane *J. Fluid Mech.* **360** 141-178
- Miesch M 2000 The coupling of solar convection and rotation-(invited review) *Solar Phys.* **192** 59-89
- Rhines P 1975 Waves and turbulence on a beta-plane *J. Fluid Mech.* **69** 417-443
- Saito N and Ishioka K 2008 Wave pattern formation from thermal convection in a horizontal shear flow *J. Japan Soc. Fluid Mech.* **27** 259-260
- Saito N and Ishioka K 2009 Interaction between a sine-type horizontal shear flow and thermal convections in a rotating system with a tilted axis *J. Japan Soc. Fluid Mech.* **28** 431-432
- Yoshikawa Y and Akitomo K 2003 Transverse roll convection in horizontal plane Couette flow *J. Fluid Mech.* **493** 191-208